Wavefront propagation by local ray tracing

Propagating wavefronts by the finite-difference method described in Chapter ?? has its limitations. Although the method gives accurate traveltimes, it produces large errors in calculating traveltime gradients when velocity varies rapidly. Because geometrical amplitudes honor the zeroth-order transport equation, which involves the traveltime gradients, these errors are reflected in the amplitude calculation. The large errors in traveltime gradients are caused by the discontinuous representation of a velocity field that the finite-difference method assumes, as well as by the first-order finite-difference approximations that the method makes.

The traveltime field in a complex velocity medium is generally a multivalued function of subsurface positions because of possible multiple arrivals. But all existing finite-difference methods compute only the traveltime of the first arrival at each subsurface point. One reason is that the wavefront of a first arrival is always continuous; hence finite-difference approximations to the eikonal equation are valid. Another reason is that among different arrivals at a subsurface point, the first arrival is easiest to identify because it has the minimum traveltime. When imaging seismic reflection data, the events corresponding to energetic arrivals should be used. However, for a complex velocity model, the energy carried by first arrivals may become considerably weaker than that carried by other later arrivals. In such a situation, the traveltimes of more energetic, later arrivals need to be computed.

This chapter introduces the local ray-tracing method for wavefront propagation. Because the method assumes a continuous velocity representation and propagates local circular wavefronts by following local rays, it gives more accurate traveltimes and amplitudes than all existing finite-difference methods. The method computes the traveltimes of multiple arrivals by disassembling a multivalued traveltime field into several single-valued fields and then computing each of them separately. These single-valued fields may include discontinuities that a finite-difference method cannot handle. The local ray-tracing method can propagate wavefronts of discontinuities.

The chapter begins with the description of a continuous representation of a velocity field. It then presents the details of the local ray-tracing method, including the local wavefront propagation scheme, the global updating scheme, and initialization. Several issues regarding multiple arrivals are also addressed. Finally, the accuracy of the method is examined, and several synthetic examples are used to demonstrate the method.

Continuous representation of a velocity field

The representation of a velocity field is crucial to the accuracy and efficiency of traveltime and amplitude calculations. Because the traveltime and amplitude calculations are more accurate in a continuous velocity model than in a discontinuous velocity model, I choose a continuous velocity representation. I map a given velocity field onto a grid formed by regular triangular cells. Within each triangular cell, velocity varies linearly, as follows:

$$v(x,z) = v_o + v_x(x - x_o) + v_z(z - z_o), \tag{1}$$

where two components of the velocity gradient are determined by

$$\begin{cases} v_x = \dfrac{(z_b - z_o)(v_a - v_o) - (z_a - z_o)(v_b - v_o)}{(z_b - z_o)(x_a - x_o) - (x_b - x_o)(z_a - z_o)} \\ \\ v_z = \dfrac{(x_a - x_o)(v_b - v_o) - (x_b - x_o)(v_a - v_o)}{(z_b - z_o)(x_a - x_o) - (x_b - x_o)(z_a - z_o)}; \end{cases} \tag{2}$$

v_o, v_a and v_b are the velocities at the three corners (x_o, z_o), (x_a, z_a) and (x_b, z_b), of the triangular cell, respectively. Figure 1 shows examples of a triangular grid and a triangular cell. With this representation, velocity is continuous everywhere, including at the boundaries of adjacent triangular cells. Velocity contrasts at the interfaces of the original velocity model are approximated by fitting triangular cells with large velocity gradients.

The reason for using linearly varying velocities within triangular cells is that seismic waves propagate along circular ray paths in a linearly varying velocity medium. Therefore, local ray-tracing in these triangular cells can be done analytically. An alternative is to use linearly varying sloth (slowness squared) within each triangular cell. The ray paths in such a medium are hyperbolas.

In a manner similar to the finite-difference method developed by Vidale (1988), two schemes need to be built for the local ray-tracing method. In the following sections, I first develop the scheme used to propagate a local wavefront through a triangular cell. I then describe the scheme that addresses the order in which the local computations proceed.

Local wavefront propagation

Local wavefront propagation is a process of propagating a wavefront to a grid point from its neighbors. Through this process, the attributes of a wavefront at a grid point are determined from the attributes of wavefronts at neighboring grid points.

The attributes of a wavefront

In a complex velocity structure, multiple arrivals may reach a subsurface point. Whereas some arrivals are identifiable by the kinematic properties of seismic waves,

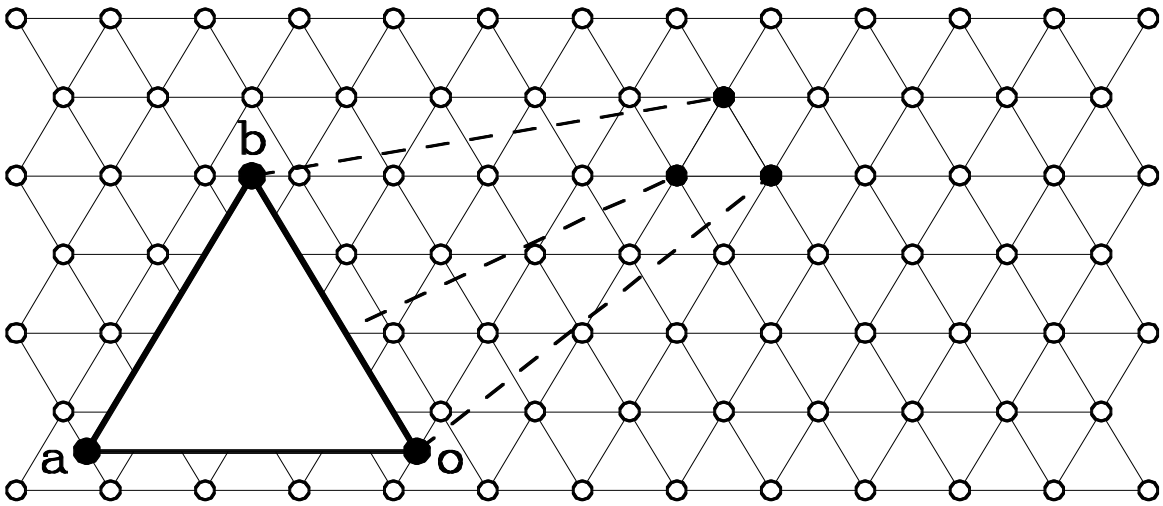

Figure 1: Examples of a triangular grid and a triangular cell. The velocity field is specified on the grid points indicated by little circles. Velocities at the three corners of a cell determine the constant velocity gradient within the cell. wftprg3-vptrigrid [ER]

others have to be identified by the dynamic properties. Therefore, the attributes of a wavefront should include both the kinematic and dynamic parameters of seismic waves.

The local ray-tracing method uses five wavefront attributes in the process of wavefront propagation. They are

$$\eta = \{\tau,\ (u,w),\ \gamma,\ R,\ J\}, \tag{3}$$

where τ is the traveltime for a wave to propagate from a surface point to a subsurface point, $(u,w) = (\tau_x, \tau_z)$ is the traveltime-gradient vector that points to the direction of the wave propagation at the subsurface point, γ is the take-off angle of the ray connecting the surface point and the subsurface point, R is the curvature radius of the wavefront at the subsurface point, and J is the geometrical spreading factor [see its definition in equation (**??**)] at the subsurface point. Among these attributes, τ, (u,w), and γ are related to the kinematic properties of wave propagation, whereas R and J are related to the dynamic properties.

Local ray-tracing

The local ray-tracing method propagates a wavefront locally through triangular cells of linearly varying velocities by following local rays. Because the whole process of wavefront propagation involves tracing many local rays, it is necessary to have an efficient ray-tracing algorithm. Fortunately, the analytical solutions to the ray equations for a linearly varying velocity field are well known, and the analytical solutions of R and J for such a velocity field are also known. Here I merely quote the results. The details of the derivations can be found in Telford et al. (1976) and Červený et al. (1977).

Suppose the attributes of a wavefront at an initial point (x_0, z_0) are known to be $\eta_0 = \{\tau_0, (u_0, w_0), \gamma_0, R_0, J_0\}$. By tracing a ray, one can find the attributes of the wavefront $\eta = \{\tau, (u, w), \gamma, R, J\}$ at an arbitrary point (x, z) on the ray. In a linearly varying velocity field, the two components of the velocity gradient (v_x, v_z) are constant. It is known that in such a velocity field the ray follows a circular trajectory. The traveltime at the point (x, z) is determined by integrating the inverse of velocity along the ray, which yields

$$\tau = \tau_0 + \frac{1}{g} \log \left(\frac{\sin i (1 + \cos i_0)}{\sin i_0 (1 + \cos i)} \right), \tag{4}$$

where $g = \sqrt{v_x^2 + v_z^2}$ is the magnitude of the velocity gradient, and i_0 and i are the ray angles shown in Figure 2. It can be shown that

$$\begin{cases} \cos i_0 &= \dfrac{v_0}{g}(v_z u_0 - v_x w_0) \\ \\ \sin i_0 &= \dfrac{v_0}{g}(v_z w_0 + v_x u_0), \end{cases} \tag{5}$$

where v_0 is the velocity at the initial point. The ray angle i at point (x, z) is related to the arc-length of the ray path as follows:

$$i = i_0 + (s - s_0) \frac{g \cos i_0}{v_0}, \tag{6}$$

where $s - s_0$ is the arc length of the ray between the two points. The two components of the traveltime gradient at the point (x, z) are determined by

$$\begin{cases} u &= \dfrac{1}{vg}(v_z \cos i + v_x \sin i) \\ \\ w &= \dfrac{1}{vg}(v_z \sin i + v_x \cos i) \end{cases} \tag{7}$$

where v is the velocity at point (x, z). Because the take-off angle of the ray does not change along the ray,

$$\gamma = \gamma_0. \tag{8}$$

Červený et al. (1977) shows that, in a velocity field of zero second-order spatial derivatives, the curvature radius of a wavefront at a point on a ray is linearly proportional to the integration of the velocity field along the ray. Because a linearly varying velocity field has zero second-order spatial derivatives, the integration of the velocity along the circular ray path gives

$$R = \frac{v_0}{v} \left[R_0 + \frac{v_0}{g \cos i_0} (1 - \frac{\cos i}{\cos i_0}) \right]. \tag{9}$$

Similarly, we can show that

$$J = J_0 \frac{vR}{v_0 R_0}, \tag{10}$$

where R is defined in equation (9).

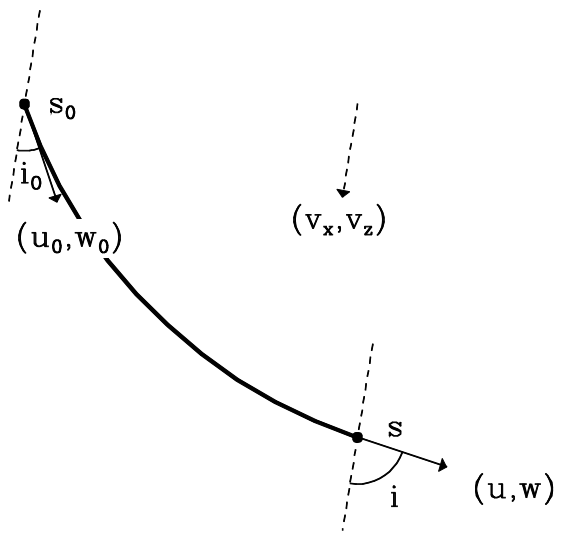

Figure 2: Ray-tracing in a constant gradient velocity field. The dashed arrow shows the direction of the velocity gradient. The solid arrows show the directions of traveltime gradients that are tangential to the ray. Ray angles are measured between the direction of the velocity gradient and the directions of the ray. wftprg3-vpraytrc [ER]

When a ray reaches the boundary of two adjacent triangular cells, the phase-matching method can be used to trace the ray across the boundary (Červený et al., 1977). Traveltime τ and take-off angle γ are always continuous across the boundary. Because of the continuous velocity representation, there is no velocity discontinuity across the boundary. Therefore the traveltime gradient (u, w) and geometrical spreading factor J are also continuous at the boundary. However, curvature radius R is generally not continuous at the boundary because of the change of the velocity gradient across the boundary. Červený et al. (1977) derived a general formula that relates the curvature radii of wavefronts on the two sides of the boundary. This general formula can be greatly simplified by considering that the velocity field is continuous at the boundary and that the boundary has zero curvature. The result is

$$R^+ = \frac{R^-}{1 + vIR^-}, \tag{11}$$

where R^+ and R^- are the curvature radii before and after crossing the boundary, respectively, and I is a factor defined as follows:

$$\begin{aligned} I &= \frac{2\tan\theta}{v^2}\left[\cos\phi(v_x^+ - v_x^-) - \sin\phi(v_z^+ - v_z^-)\right] + \\ &\quad \frac{\tan^2\theta}{v^2}\left[\sin\phi(v_x^+ - v_x^-) + \cos\phi(v_z^+ - v_z^-)\right]. \end{aligned}$$

As shown in Figure 3, θ is the incident angle of the ray to the normal of the boundary, ϕ is the angle between the orientation of the boundary and the z-axis, and (v_x^-, v_z^-) and (v_x^+, v_z^+) are the velocity gradients of two adjacent cells, respectively.

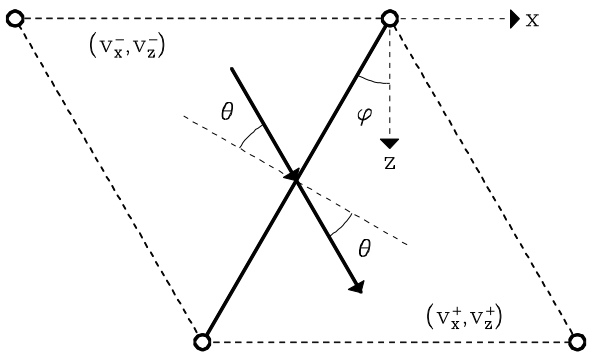

Figure 3: Ray-tracing across a boundary of two triangular cells. Because the velocity is continuous at the boundary, the angle of incidence is equal to the angle of refraction. wftprg3-vpbound [ER]

Propagating local circular wavefronts

A wavefront can be locally propagated by tracing local rays. Figure 4 shows a cell in a triangular grid. At two corners of the triangular cell, a and b, the attributes of the wavefront are known to be

$$\eta_a = \{t_a, (u_a, w_a), R_a, \gamma_a, J_a\}$$

and

$$\eta_b = \{t_b, (u_b, w_b), R_b, \gamma_b, J_b\},$$

respectively. At the third corner o, the wavefront attributes,

$$\eta_o = \{t_o, (u_o, w_o), R_o, \gamma_o, J_o\},$$

are unknown and to be determined through a procedure of propagating a local wavefront that passes the line boundary between points a and b.

The procedure begins with local ray-tracing from points a and b, where the wavefront attributes are known. As shown in Figure 4, ray a shoots from point a and in the direction of the gradient vector (u_a, w_a), and ray b shoots from point b and in the direction of the gradient vector (u_b, w_b). These two rays form a ray-tube that guides the propagation of the local wavefront confined between points a and b. If a point on the local wavefront follows the wavefront propagation and reaches point o, it must cross the boundary ab and propagate through the triangular cell. Therefore, the two local rays are traced as if the straight-line boundary ab extends out at both ends and the velocity field within the triangular cell extends out with the velocity gradient unchanged. The wavefront attributes at any point on the two rays can be calculated by using the formulas presented in Section

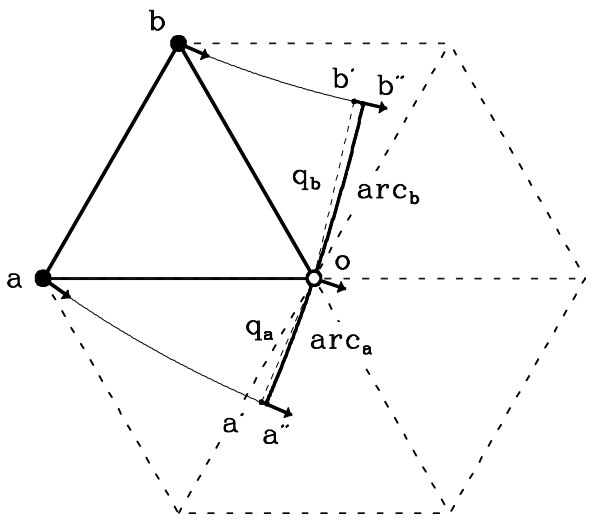

Figure 4: Local wavefront propagation when the wavefront attributes at points a and b are associated with a common wavefront. By tracing two local rays, the wavefront attributes at point o is determined jointly from the wavefront attributes at points a and b. wftprg3-vpwftprg1 [ER]

As shown in Figure 4, the local rays a and b are traced to points a' and b', respectively. At these two points, the normal distances from the third corner of the triangular cell, o, to the two rays are achieved. Let q_a and q_b denote the two normal distances, and define

$$\begin{aligned} q_a &= v_{a'} w_{a'} (x_{a'} - x_o) - v_{a'} u_{a'} (z_{a'} - z_o) \\ q_b &= v_{b'} w_{b'} (x_{b'} - x_o) - v_{b'} u_{b'} (z_{b'} - z_o), \end{aligned}$$

where (x_o, z_o) are the coordinates of the third corner of the triangular cell, and $(v_{a'} u_{a'}, v_{a'} w_{a'})$ and $(v_{b'} u_{b'}, v_{b'} w_{b'})$ are the unit vectors tangential to the rays at the normal points $(x_{a'}, z_{a'})$ and $(x_{b'}, z_{b'})$, respectively. With this definition, the normal distance is positive when a ray is on one side of point o, and negative when a ray is on the other side. To ensure that the attributes of the wavefront at the point (x_0, z_0) is computed by propagating the local wavefront passing the line boundary between points a and b, it is required that the point (x_o, z_o) is within the ray tube formed by the two rays. This condition is satisfied when $q_a \leq 0$ and $q_b \geq 0$.

Because the normal points a' and b' are on the rays, the attributes of the wavefront at these points can be computed analytically. Let $R_{a'}$ be the curvature radius of the wavefront at the normal point a'. Then, the curvature center of the wavefront at this point is

$$\begin{cases} x_{a0} = x_{a'} - v_{a'} u_{a'} R_{a'} \\ z_{a0} = z_{a'} - v_{a'} w_{a'} R_{a'}. \end{cases} \tag{12}$$

Similarly, the curvature center of the wavefront at the normal point b' is

$$\begin{cases} x_{b0} &= x_{b'} - v_{b'} u_{b'} R_{b'} \\ z_{b0} &= z_{b'} - v_{b'} w_{b'} R_{b'}, \end{cases} \tag{13}$$

where $R_{b'}$ is the curvature radius of the wavefront at that point.

The local wavefront within the ray tube formed by the rays a and b is considered to be continuous if one of the following two sets of conditions is satisfied:

1. $R_{a'} > 0$, $R_{b'} > 0$ and $w_{a'} u_{b'} - u_{a'} w_{b'} > 0$.
2. $R_{a'} < 0$, $R_{b'} < 0$ and $w_{a'} u_{b'} - u_{a'} w_{b'} < 0$.

The first set of conditions defines a divergent local wavefront, the second set a convergent local wavefront. Figure 5 displays examples of these two cases. If neither of the two sets of conditions holds, the local wavefront is considered to be discontinuous. Figure 6 displays two examples of discontinuous local wavefronts.

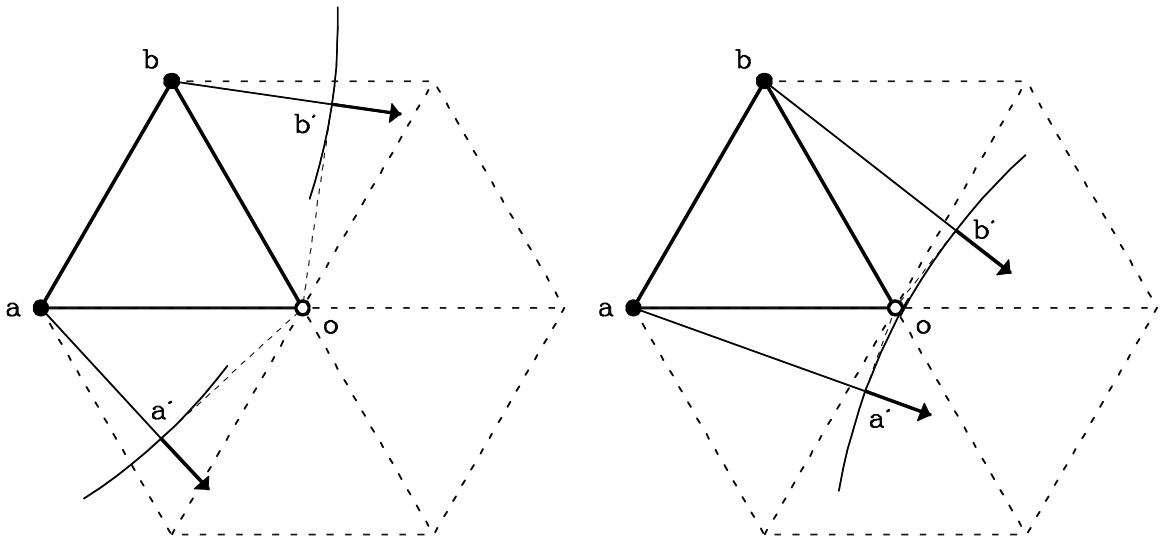

Figure 5: Two examples of continuous local wavefronts. Left: a divergent local wavefront. Right: a convergent local wavefront. wftprg3-vpwptype1 [ER]

When the local wavefront is continuous, the attributes at points a and b are associated with a common wavefront. Therefore, the curvature center of the wavefront at point o is estimated by averaging the curvature centers of the wavefront at points a' and b' as follows:

$$\begin{cases} x_{o0} &= \alpha x_{a0} + \beta x_{b0} \\ z_{o0} &= \alpha z_{a0} + \beta z_{b0}, \end{cases} \tag{14}$$

where α and β are weighting coefficients determined by the normal distances, as follows:

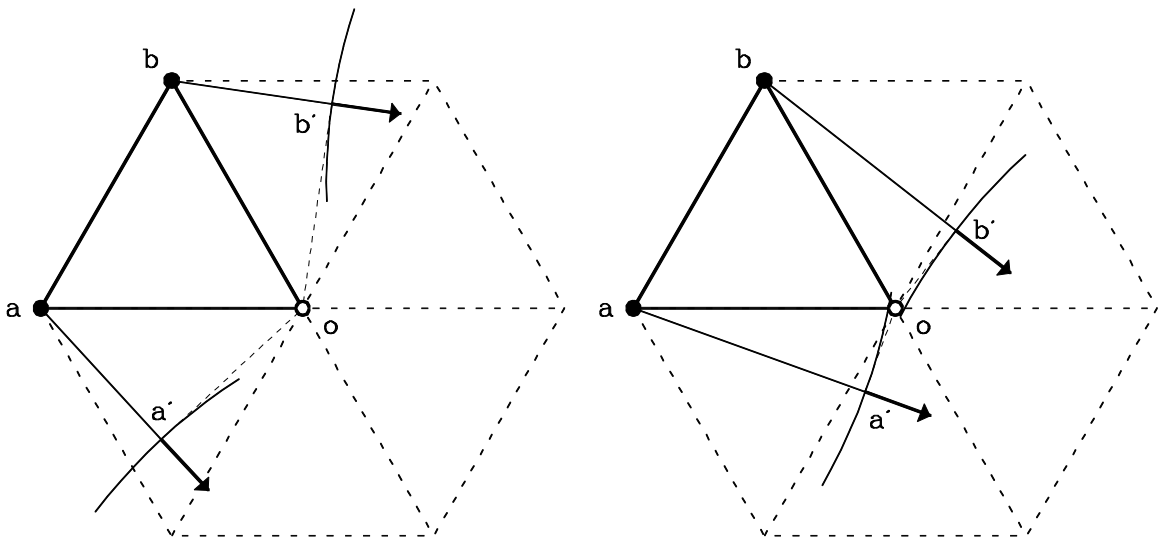

Figure 6: Two examples of discontinuous local wavefronts. wftprg3-vpwptype2 [ER]

$$\begin{cases} \alpha &= \dfrac{|q_b|}{|q_b| + |q_a|} \\ \\ \beta &= \dfrac{|q_a|}{|q_b| + |q_a|}. \end{cases} \tag{15}$$

The curvature radius of the wavefront at point o is then computed by

$$R_o = \text{sgn}(R_{a'} + R_{b'})\sqrt{(x_o - x_{o0})^2 + (z_o - z_{o0})^2}, \tag{16}$$

and two components of the traveltime gradient by

$$\begin{cases} u_o &= \dfrac{(x_o - x_{o0})}{v_o R_o} \\ \\ w_o &= \dfrac{(z_o - z_{o0})}{v_o R_o}, \end{cases} \tag{17}$$

where v_o is the velocity at point o.

The true wavefront at point o is approximated by a local circular wavefront of radius R_o and centered at (x_{o0}, z_{o0}). As shown in Figure 4, the local circular wavefront at the point o intersects with ray a at point a'' and ray b at point b''. Because these two points are on the rays, the attributes of the wavefronts can be calculated analytically. Let $t_{a''}$ and $t_{b''}$ be the traveltimes at two intersections. Because both point a'' and point b'' are on the local circular wavefront defined at the point o, the weighted average of $t_{a''}$ and $t_{b''}$ is used to estimate the traveltime at point o; that is

$$t_o = \alpha t_{a''} + \beta t_{b''} \tag{18}$$

where α and β are defined in equation (15). It can be shown that in a linearly varying velocity field the geometrical spreading factor J varies along a wavefront in proportion to the velocity. Therefore, the estimate of the geometrical spreading factor J_o from the attributes at point a'' is $v_o J_{a''}/v_{a''}$ and at point b'' is $v_o J_{b''}/v_{b''}$. Averaging the two gives

$$J_o = \alpha \frac{v_o}{v_{a''}} J_{a''} + \beta \frac{v_o}{v_{b''}} J_{b''} \tag{19}$$

The last parameter to be estimated is the take-off angle of the ray that reaches point o. It can be shown that, in 2-D

$$J = \frac{\partial \gamma}{\partial n},$$

where n is the distance normal to the ray. Therefore,

$$\begin{aligned} \Delta\gamma &= \int \frac{1}{J} dn \\ &\approx \frac{1}{\bar{J}} \Delta\text{arc}, \end{aligned}$$

where $\bar{J}$ is the average geometrical spreading factor over the arc length Δarc. If the average of J_o and $J_{a''}$ is used to approximate the $\bar{J}$ over arc_a and the average of J_o and $J_{b''}$ over arc_b, then γ_o is estimated by weighted averaging as follows:

$$\gamma_o = \alpha \left(\gamma_{a''} - \frac{2\text{arc}_a}{J_o + J_{a''}} \right) + \beta \left(\gamma_{b''} - \frac{2\text{arc}_b}{J_o + J_{b''}} \right). \tag{20}$$

With equations (16) to (20), one can compute the attributes of the wavefront at point o, the third corner of the triangular cell.

When the local wavefront is discontinuous, the attributes at points a and b are associated with different wavefronts. Therefore the local wavefront at each point should be propagated individually. Figure 7 shows an example in which the local wavefront at point b is propagated. In this case, the curvature center of the wavefront at point o is assumed to coincide with the curvature center of the wavefront at point b', that is, $x_{o0} = x_{b0}$ and $z_{o0} = z_{b0}$. The curvature radius is then

$$R_o = \text{sgn}(R_{b'}) \sqrt{(x_o - x_{o0})^2 + (z_o - z_{o0})^2}. \tag{21}$$

The formula for computing the components of the traveltime gradient at point o is identical to equation (17). The traveltime t_o, geometrical spreading factor J_o, and take-off angle γ_o are computed by simply setting $\alpha = 0$ and $\beta = 1$ in equations (18), (19), and (20).

There are two special cases in which the rays a and b do not form a ray-tube because of multiple arrivals. Figure 8 shows examples of two such cases. In both cases, the rays a and b converge; that is

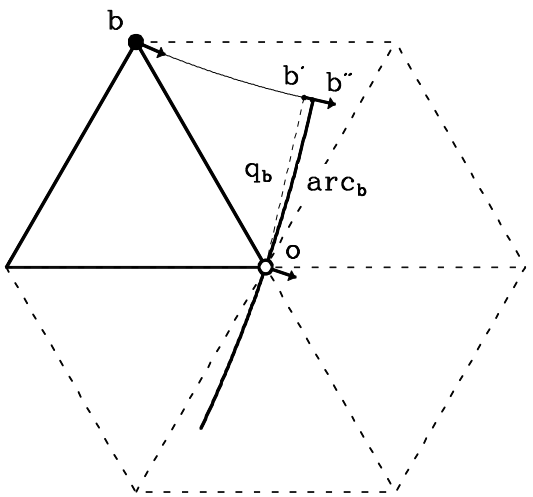

Figure 7: The local wavefront propagation when the wavefront attributes at points a and b are associated with different wavefronts. The wavefront attributes at point o are determined separately from the wavefront attributes at each point (point b is an example) separately. wftprg3-vpwftprg2 [ER]

$$w_{a'}u_{b'} - u_{a'}w_{b'} < 0.$$

The first case has $q_a < 0$ and $q_b < 0$. Ray a guides the propagation of the local wavefront passing between points a and b, whereas ray b guides the propagation of another local wavefront that does not pass between points a and b. Therefore, only ray a is used to compute the attributes of the wavefront at point o. The second case has $q_a > 0$ and $q_b > 0$, and ray b, instead of ray a, is used in the computation.

The wavefront may be diffracted at points a and b because of the changes of the velocity gradients in adjacent triangular cells. Figure 9 shows an example of diffraction at point b. Two rays that are traced with the same initial conditions at point b, but different velocity gradients diverge and form a ray fan. The local wavefront corresponding to diffraction is defined between the two rays. The attributes of the diffracted wavefront at point o are computed by tracing the local ray connecting points b and o.

The global updating scheme

With the local computations for propagating wavefronts, the attributes of wavefronts can be found throughout the grid by following a global updating scheme. The global updating scheme describes the order in which the local wavefront propagation proceeds. This section presents a scheme that assumes a point source on the earth's surface. However, it is not difficult to generalize the scheme to an arbitrary source position.

Initialization

Since a triangular grid is used, the process of wavefront propagation proceeds conveniently on an expanding half-hexagonal ring centered at the source point. To

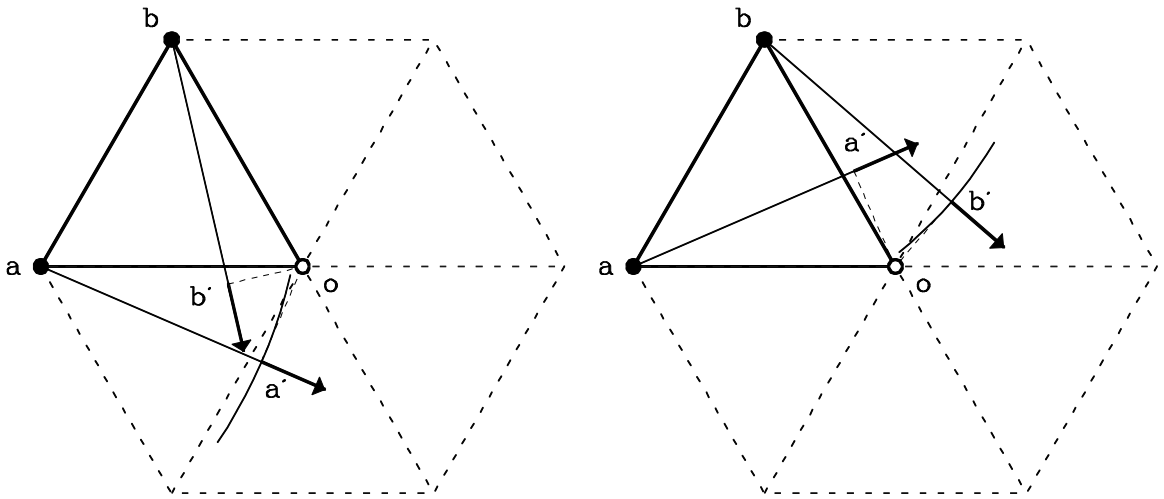

Figure 8: Two examples of local wavefronts of multiple arrivals. Left: only ray a is used to propagate the local wavefront. Right: only ray b is used to propagate the local wavefront. wftprg3-vpwptype3 [ER]

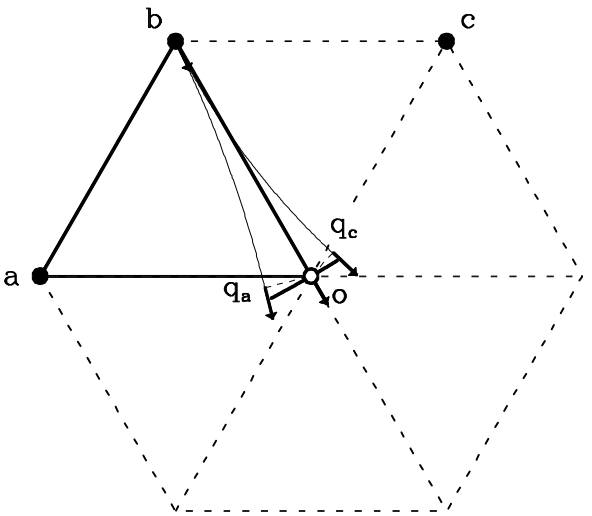

Figure 9: An example of a local wavefront diffracted at point b. Two rays that are traced with the same initial conditions, but different velocity gradients diverge and form a ray fan. The diffracted local wavefront propagates by following the expansion of the ray fan. wftprg3-vpwftprg3 [ER]

start the process, the attributes of wavefronts are initialized at the grid points inside and on a half-hexagonal ring shown in Figure 10. The radius of this half-hexagonal ring is chosen to be the radius of the largest half-hexagon within which the velocity field is well approximated by a linear function. Such a choice makes it possible to compute analytically the attributes of wavefronts at the grid points inside and on this half-hexagonal ring.

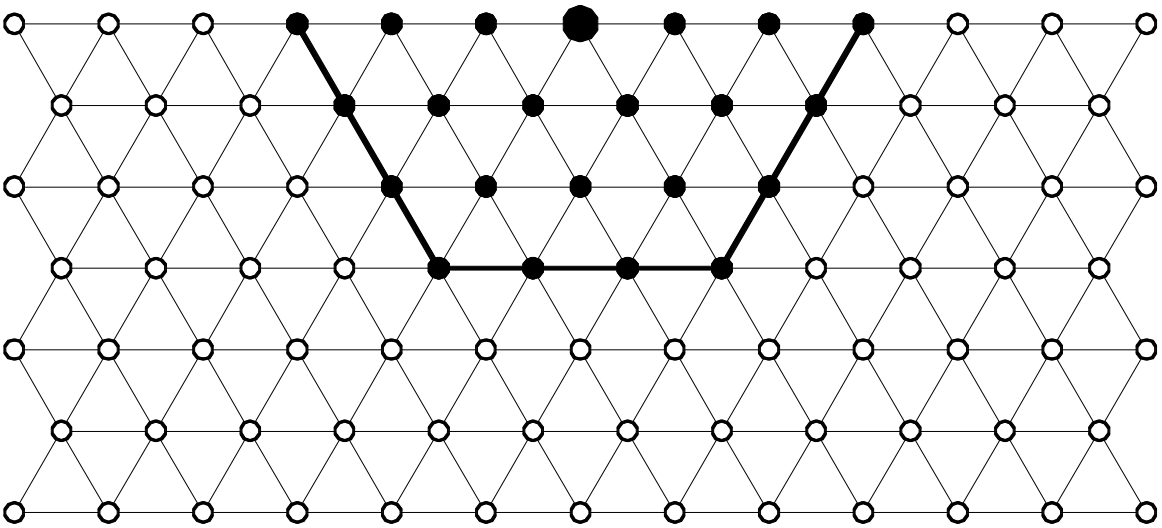

Figure 10: The initialization of wavefront propagation. The attributes of wavefronts are initialized at the grid points inside and on a half-hexagonal ring of radius 3 (indicated by thick lines), as indicated by the small black dots. The large black dot indicates the source point. wftprg3-vpinit [ER]

Three phases of the updating scheme

From the initial half-hexagonal ring on which the attributes of wavefronts are computed analytically, the process of wavefront propagation follows the expansion of the ring step by step. Suppose that the attributes of the wavefronts are known at all the grid points inside and on the half-hexagonal ring of radius 4, as indicated by small black dots in Figure 11. At the grid points on the three sides of the half-hexagon of radius 5 (indicated by thick lines), the attributes of the wavefronts are unknown and are to be computed by one step of the updating scheme. I refer to these grid points as *target points* (indicated by small squares). Each target point has six triangular cells attached to it. Each of these triangular cells has one boundary across which a local wavefront may propagate toward the target point. Figure 11 shows an example in which six boundaries associated with a target point (indicated by a fat square) are labeled from 1 to 6. Because seismic waves seldom propagate towards the source point, it is reasonable to assume that no local wavefront propagates into the half-hexagonal ring of radius 5 (thick lines in Figure 11) from outside. According to this assumption, local wavefronts that reach the target point must pass the boundaries 1, 2, or 3 shown in Figure 11. Therefore, one step of the updating scheme consists of three phases. In the first phase, the local wavefront passing the boundary 1 is

propagated. The second and third phases propagate the local wavefronts passing the boundaries 2 and 3, respectively. Each phase also involves the process of checking the possible diffractions at the two ends of the corresponding boundary (see the example shown in Figure 9).

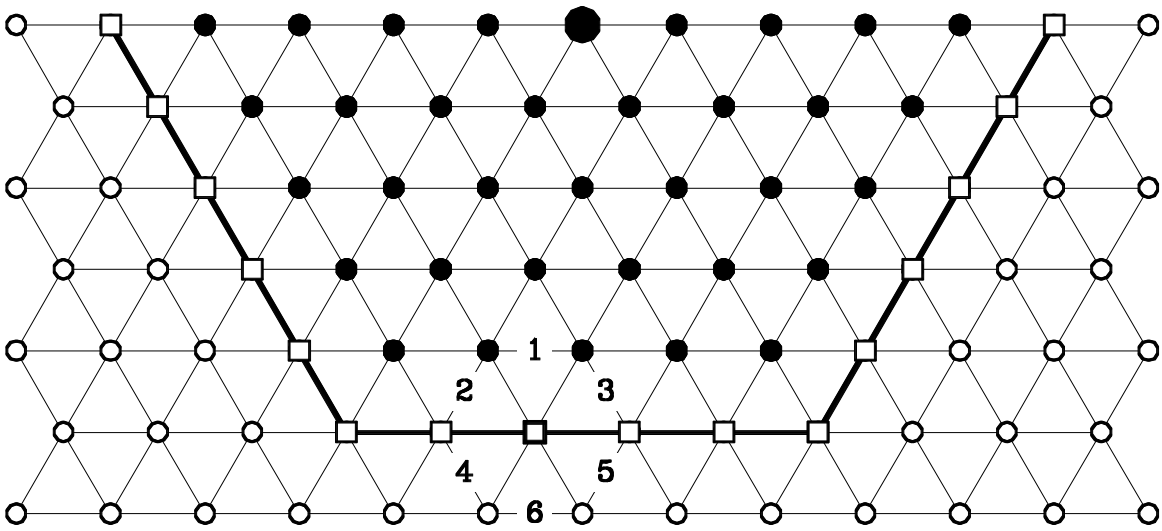

Figure 11: The attributes of wavefronts are known at the grid point inside and on the half-hexagonal ring of radius 4, which are indicated by small black dots. The large black dot indicates the source point. The target points located along the three sides of the half-hexagonal ring of radius 5 (thick lines) are indicated by small square. Six boundaries associated with a target point (indicated by a fat square) are labeled from 1 to 6. wftprg3-vpgus [ER]

Figure 12 shows how the wavefront propagation in each of the three phases proceeds globally. Because the boundary 1 associated with each target point is always on the half-hexagonal ring of radius 4, the wavefront attributes are known at the two ends of the boundary. Therefore, in the first phase, local wavefronts are propagated toward the corresponding target points independently. The situation is different in the second phase. For each target point, one end of boundary 2 is at another target point, where the attributes of wavefronts may be unknown. Therefore, local wavefronts are propagated sequentially and counter-clockwise, as shown in Figure 12. The propagation of a local wavefront is initiated at a target point when the attributes of the wavefronts are known at both ends of the boundary 2 associated with the target point. The propagation terminates at a target point when the attributes of wavefronts are unknown at one end of the boundary 2. The initiation and termination of the local wavefront propagation may repeat several times along the half-hexagonal ring. Similarly, in the third phase, local wavefronts are also propagated sequentially, but clockwise.

After the three phases of wavefront propagations, the attributes of wavefronts at all target points are computed. The half-hexagonal ring increases its radius by one grid size for the computation of the next step. This process is repeated until the expanded half-hexagonal ring covers all the grid points of the given model.

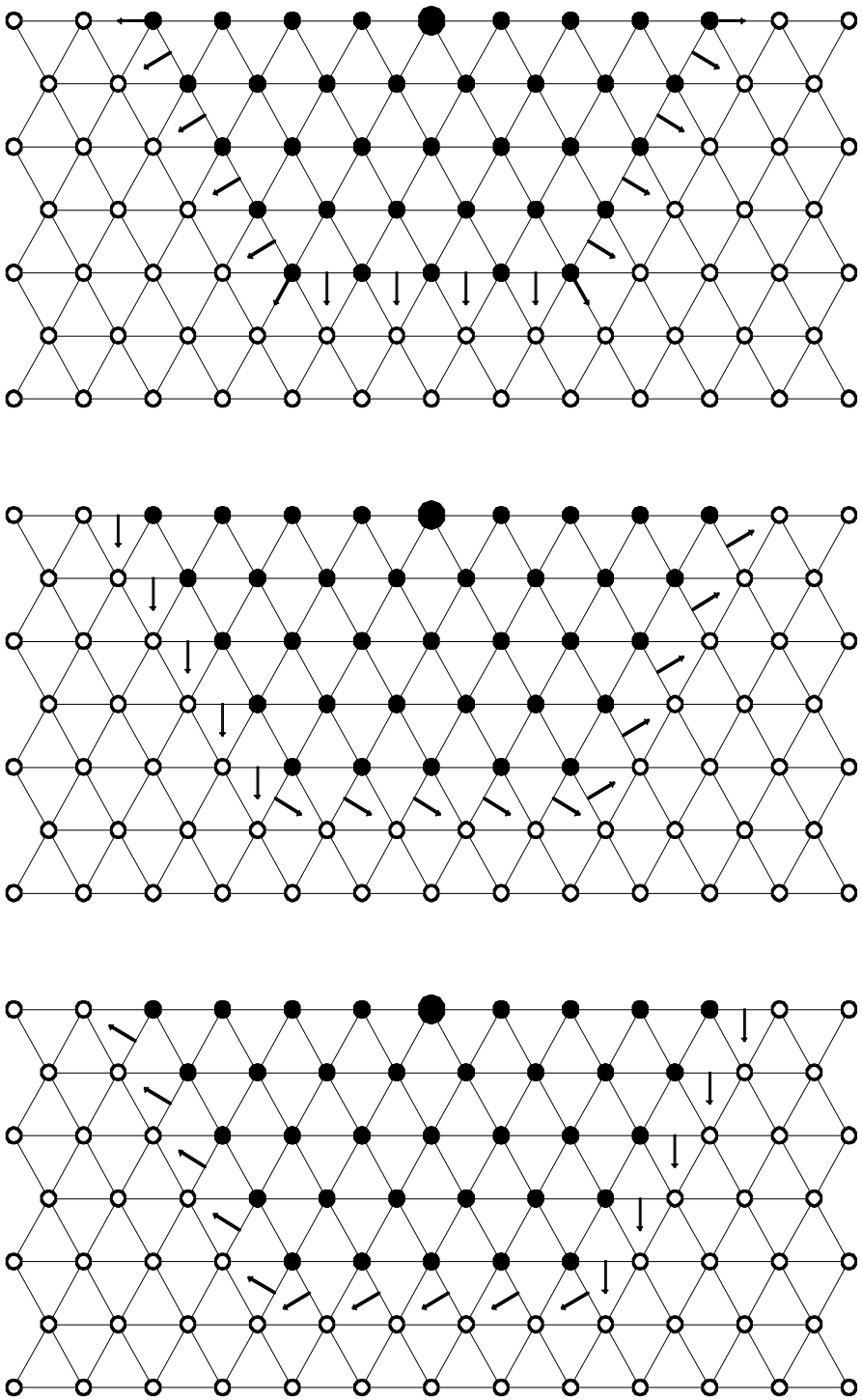

Figure 12: Three phases of the global updating scheme in one step of wavefront propagation. Top: propagating out. Middle: propagating counter-clockwise. Bottom: propagating clockwise. The big black dot shows the source position. The small black dots inside and on the half-hexagonal ring of radius 4 show the grid points at which the attributes of the wavefront are known. The arrows show that the local wavefronts passing the boundaries attached to the ends of the arrows are propagated toward the grid points the arrows point to. wftprg3-vpupdate [ER]

Multiple arrivals

When a grid point has multiple arrivals, the three phases of wavefront propagation give different results regarding the attributes of wavefronts. The following rules are used to select a specific arrival:

- For first arrivals, select minimum t_o.
- For most energetic arrivals: select minimum J_o.
- For left-going arrivals: select minimum u_o.
- For right-going arrivals: select maximum u_o.
- For up-going arrivals: select minimum w_o.
- For down-going arrivals: select maximum w_o.

Because these rules are defined locally, they don't generally ensure the global selection. The first arrival is an exception. Selecting minimum traveltimes at every step of the local wavefront propagation yields global minimum traveltimes. This result can be explained by the fact that traveltime is a monotonically increasing function along a ray. Other attributes of wavefronts do not have this property. For example, the geometrical spreading factor J may increase or decrease along a ray. Thus, the method may give the locally most energetic arrivals, instead of the globally most energetic arrivals.

Numerical results

Using synthetic velocity models, I first examine the accuracy of the local ray-tracing method by comparing its results with either the analytical solutions or the results of wave-equation modeling. I then show the results of the traveltime calculations for multiple arrivals.

Accuracy

I examine the accuracy of the local ray-tracing method with three synthetic velocity models. The first is a constant gradient velocity model in which velocity increases linearly from 2. km/s at the surface to 8. km/s at the depth of 2. km. This model is similar to the one used for testing the accuracy of the finite-difference method described in Chapter **??** with the exception that the velocity gradient is doubled. The local ray-tracing method is used to calculate the attributes of wavefronts in this model. In the calculations, the grid size is 20 m. The top panel of Figure 13 shows the contour lines of the traveltime field, plotted on the top of the velocity displays. The contour lines of the traveltime field display the trajectories of the wavefronts. Because of the increase in velocity with depth, the wavefronts are stretched downward. Since the analytical solution of the traveltime field is known for such a linearly

increasing velocity field, it is used to check the accuracy of the computation. The bottom panel of Figure 13 shows the differences between the analytical solution and the traveltime field calculated by the local ray-tracing method. The maximum error is less than 0.01 ms, which is much smaller than the maximum error produced by the finite-difference method. Similarly to Figure 13, Figures 14, 15 and 16 show the results of the calculation for take-off angles, curvature radii of wavefronts and geometrical spreading factors, respectively, which are accurate enough for Kirchhoff depth migration of seismic reflection data recorded at the earth's surface.

The second and third synthetic velocity model is a constant velocity field of 3 km/s with a 50% negative or positive Gaussian anomaly, respectively, as shown in Figure 17. The size of anomalies is about 200 meters. I use the local ray-tracing method to compute the traveltime field of first arrivals in these models. The grid size used in the computations is 20 meters. In Figure 17, I compare the results of the traveltime calculations with the wave fields simulated by wave-equation modeling. Because a minimum-phase wavelet is used in the wave-equation modeling, the contour lines of the traveltime fields closely follow the first breaks of the wavelets along the first arrival in the corresponding snapshots of the wave fields.

Multiple arrivals

I illustrate the traveltime calculation for multiple arrivals with three different velocity models. The first model is identical to the one shown in the top-left panel of Figure 17, a constant velocity field of 3 km/s with a 50% negative Gaussian anomaly. I simulated the wave field in such a velocity field by wave-equation modeling. Two panels in Figure 18 displays a snapshot of the wave field at 0.48 second. After propagating through the negative anomaly, the wavefront forms a triplication. Overlain on these panels are the 0.48s-contour of the traveltime fields calculated by selecting left-going arrivals and right-going arrivals, respectively. It can be seen that parts of the contour lines closely follow the left-going or right-going arrivals that are not first arrivals.

The second velocity model is a two-layer model. The velocities are 1.5 km/s in the top layer and 4.5 km/s in the bottom layer. After the critical angle, each point in the top layer has two arrivals: an arrival propagating directly from the source and an arrival refracted at the interface between two layers. Therefore, the traveltime field is multivalued in this region. I compute the traveltime field of multiple arrivals by applying the local ray-tracing method with three different selections: the first one selects the first arrivals, the second one selects the most energetic arrivals, and the third one selects up-going arrivals. Figure 19 shows the contours of the three single-valued traveltime fields. In the top layer, the first arrivals are the combinations of direct arrivals and diffracted arrivals, the most energetic arrivals are purely direct arrivals, and the upgoing arrivals have more diffracted arrivals than the first arrivals. The three traveltime fields are identical in the bottom layer because there each point has only one arrival. The discontinuities of the wavefronts are easy to identify in the traveltime fields of the most energetic arrivals and upgoing arrivals. Figure 20

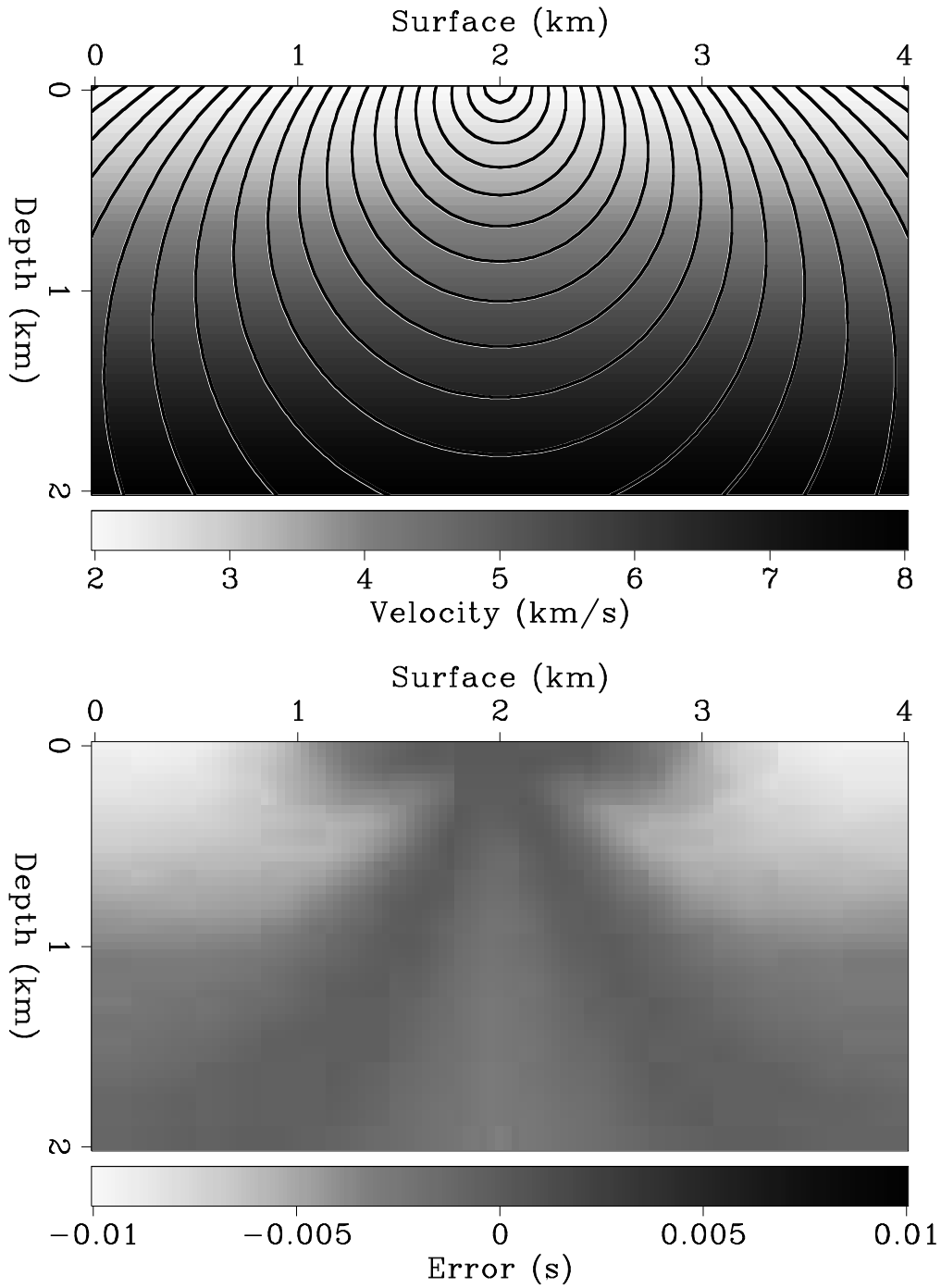

Figure 13: The traveltime calculation for a constant gradient velocity model. The background of the top panel shows the velocity field. The source is on the surface in the center of the model. Overlain on the top panel are the contour lines of the traveltime field with 0.04 second intervals. The bottom panel shows the error distribution of the calculation. wftprg3-ttmgra [ER]

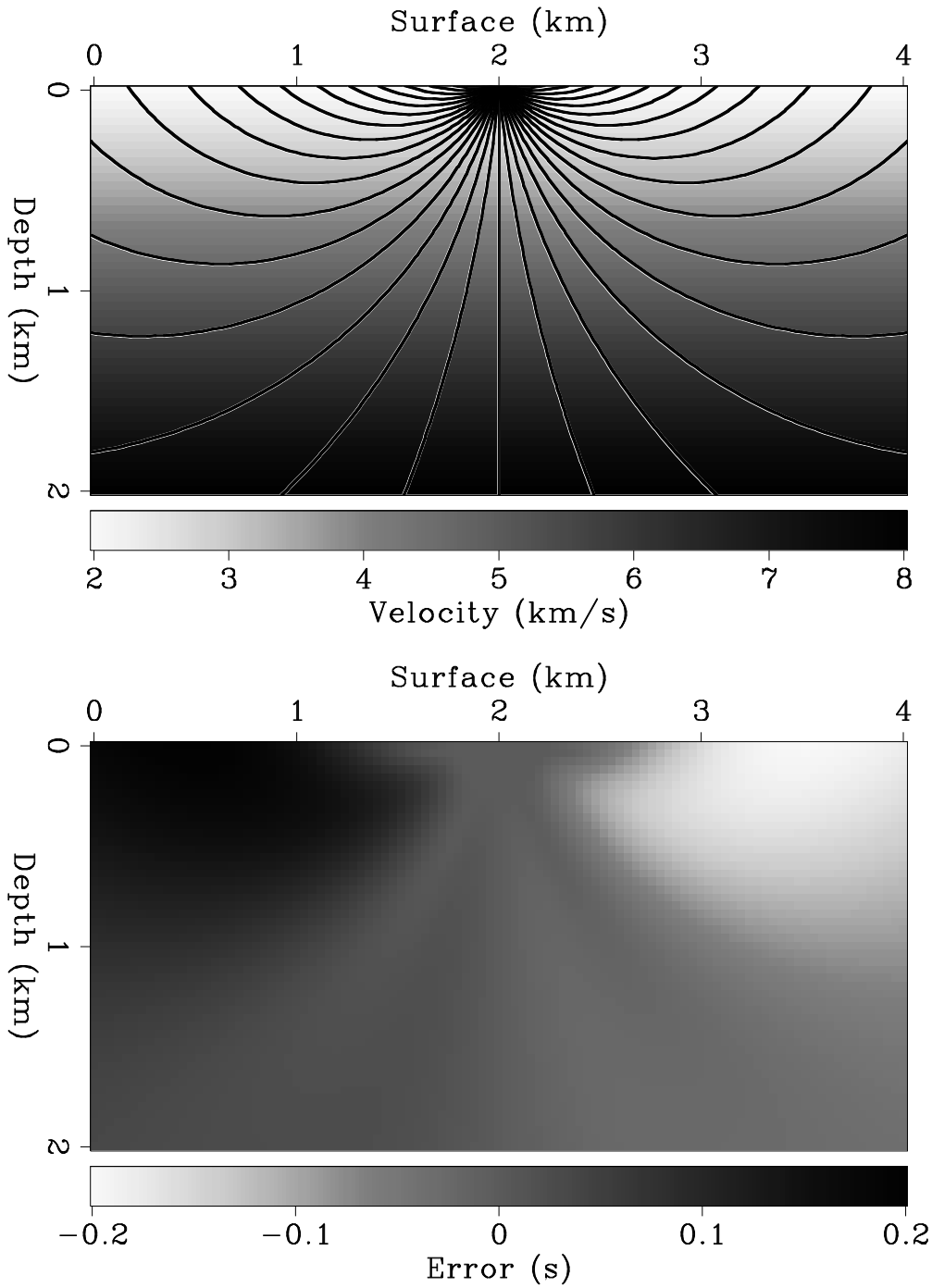

Figure 14: The take-off angle calculation for a constant gradient velocity model. The background of the top panel shows the velocity field. The source is on the surface in the center of the model. Overlain on the top panel are the contour lines of the take-off angle field with 5 degree intervals. The bottom panel shows the error distribution of the calculation. wftprg3-thgra [ER]

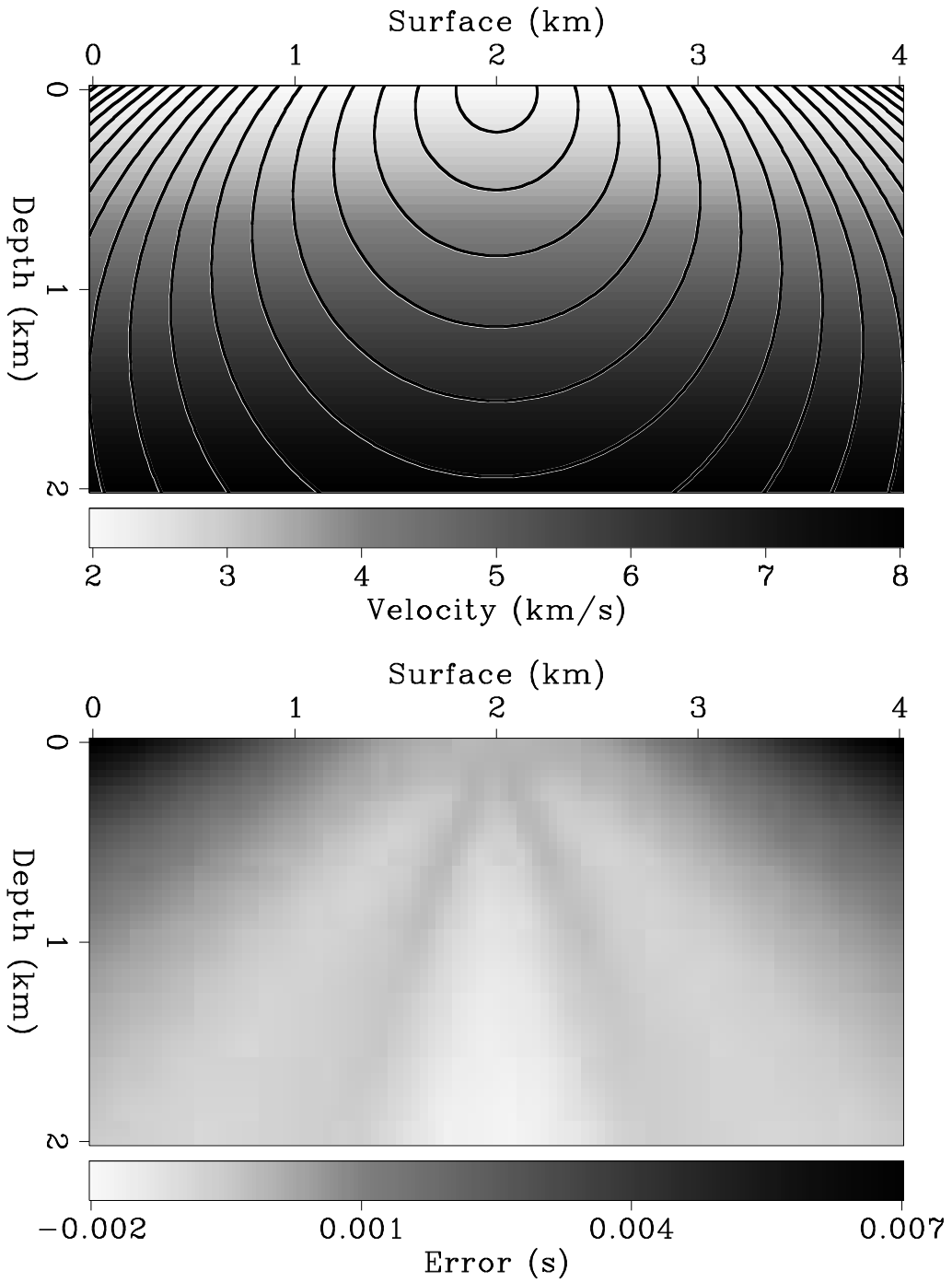

Figure 15: The curvature-radii of wavefronts for a constant gradient velocity model. The background of the top panel shows the velocity field. The source is on the surface in the center of the model. Overlain on the top panel are the contour lines of the curvature-radius field of wavefronts with 0.2 km intervals. The bottom panel shows the error distribution of the calculation. wftprg3-rgra [ER]

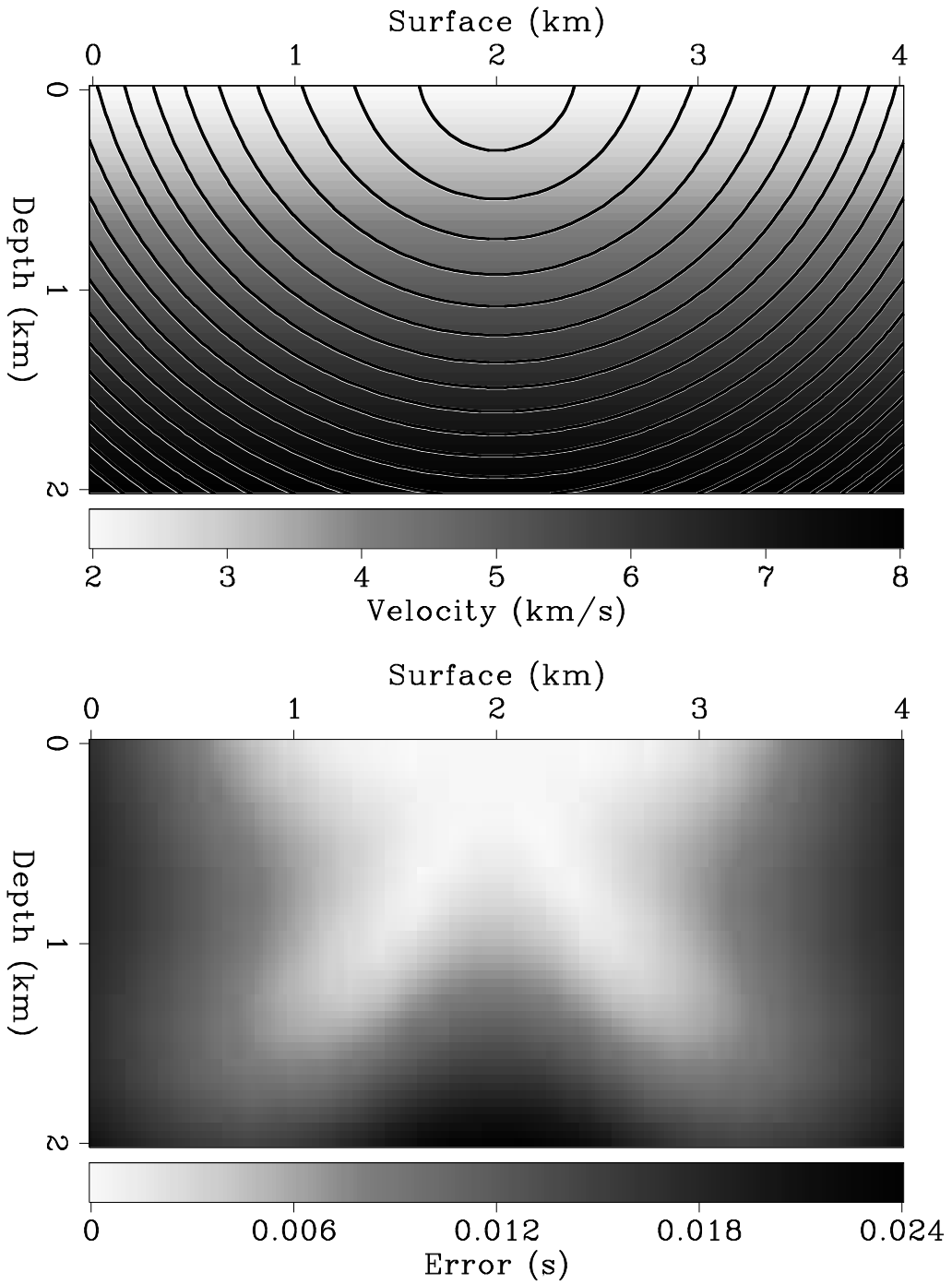

Figure 16: The geometrical spreading factors for a constant gradient velocity model. The background of the top panel shows the velocity field. The source is on the surface in the center of the model. Overlain on the top panel are the contour lines of the traveltime field with 0.4 km intervals. The bottom panel shows the error distribution of the calculation. wftprg3-jjgra [ER]

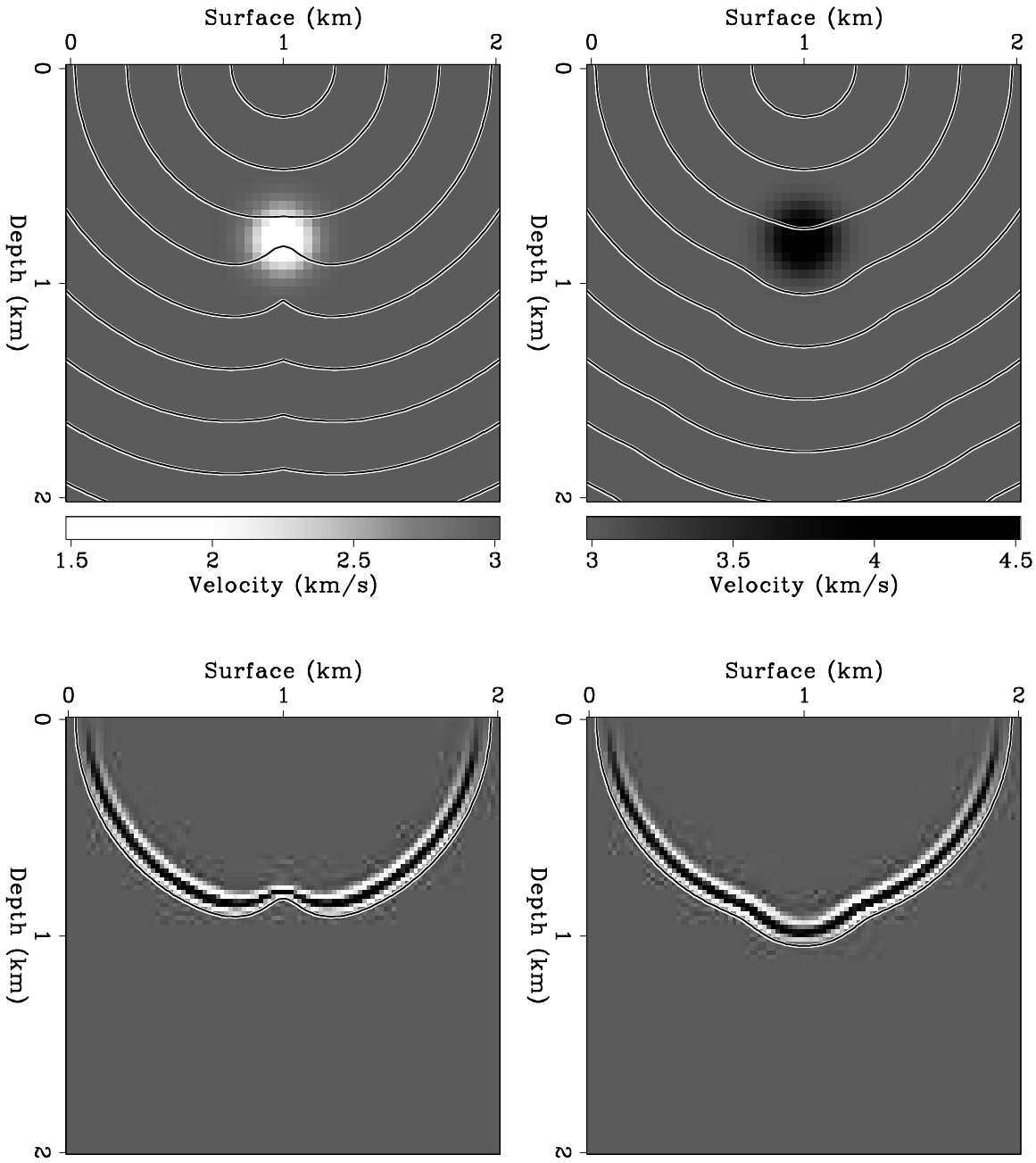

Figure 17: The traveltimes of first arrivals in velocity models with a negative Gaussian anomaly (left) and a positive anomaly (right). The backgrounds of the top panels show the velocity fields. Overlain are the contour lines of the traveltime fields. The contour intervals are 0.08 second. The bottom panel compares the wave fields simulated by wave-equation modeling with the traveltime field calculated by the local ray-tracing method. The intensity plots show snapshots of the wave fields at 0.32 second; the overlain curves are the 0.32s-contour lines of the traveltime fields. wftprg3-twpn [ER]

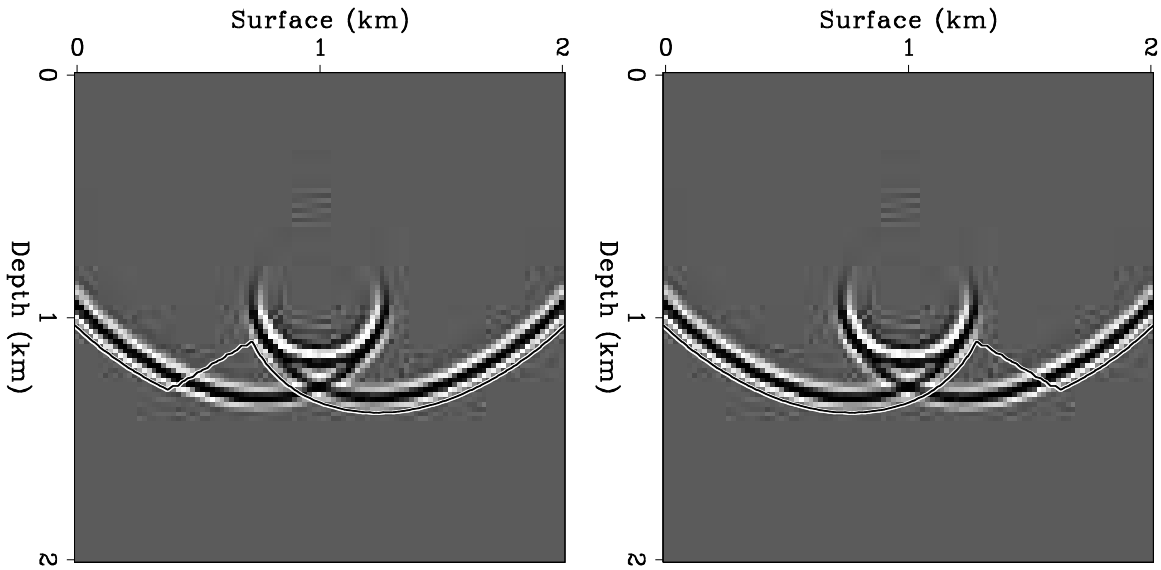

Figure 18: The traveltimes of left-going (left) or right-going (right) arrivals in a velocity model with a negative Gaussian anomaly. The intensity plots display a snapshot of the wave field simulated by wave-equation modeling. Overlain are the contour lines of the traveltime time field calculated by the local ray-tracing method. wftprg3-twlr [ER]

compares the results calculated by the local ray-tracing method with the wave field simulated by the wave-equation modeling. Because a minimum-phase wavelet is used in wave-equation modeling, the contour lines of the traveltime fields closely follow the first breaks of the wavelets in the corresponding snapshots of the wave fields.

As a final experiment, I compute the traveltime field in the Marmousi model shown in Figure 21. This synthetic velocity model has a complex geological structure with large velocity contrasts. Many regions in the model have multiple arrivals. The computation is conducted on a triangular grid with a grid size of 16 meters. Figure 21 shows the traveltime field of first arrivals in the Marmousi model. The contour plot shows that the circular wavefronts generated at the source point are severely distorted after propagating through the complex structure. The wavefronts propagate rapidly in several thin layers of high interval velocities. The comparison with the wave field computed by wave-equation modeling confirms the accuracy of the local ray-tracing method. This experiment also shows that the local ray-tracing method is robust.

Figure 21 indicates that the first arrivals at some regions are considerably weaker than later arrivals. Therefore, I compute another traveltime field by selecting the most energetic arrivals. As shown in Figure 22, the result with this model is not completely satisfactory. Although energetic arrivals at the shallow regions of the model are correctly computed, the method still picks up the weak arrivals diffracted at the boundaries of thin high-velocity layers. An explanation of this result is that the local ray-tracing method does not ensure global selection. Weak arrivals propagating in thin high-velocity layers may be strong at an early stage of the propagation.

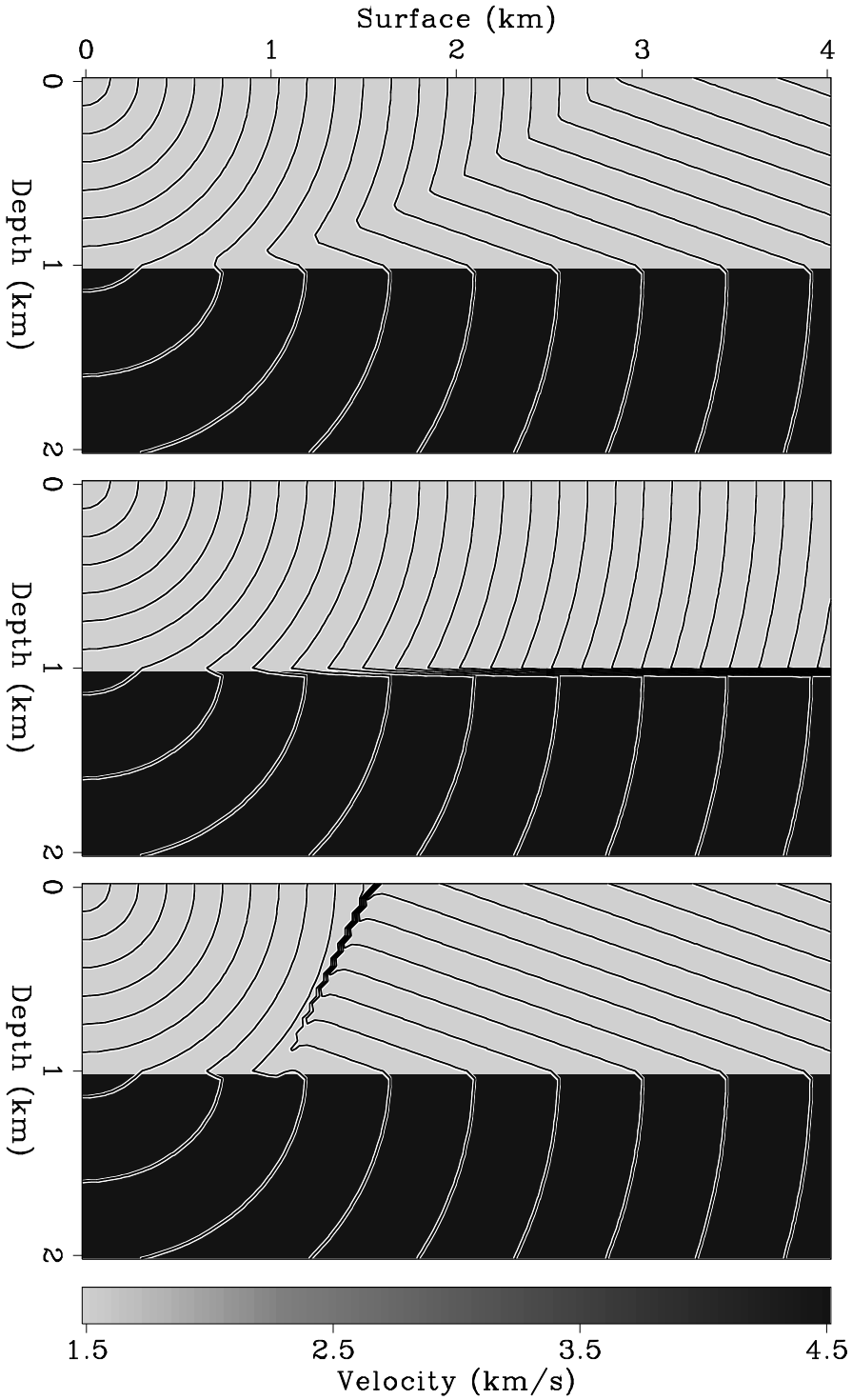

Figure 19: The traveltimes of multiple arrivals in a two-layer model. A point source positioned at the upper-left corner of the model generates a multivalued traveltime field in the top layer. This field is disassembled into three single-valued traveltime fields corresponding to first arrivals (top), most energetic arrivals (middle), and up-going arrivals (bottom). The contour lines of three single-valued traveltime fields are plotted on the intensity backgrounds showing the velocity field. The contour interval is 0.1 second. wftprg3-ttmlay [ER]

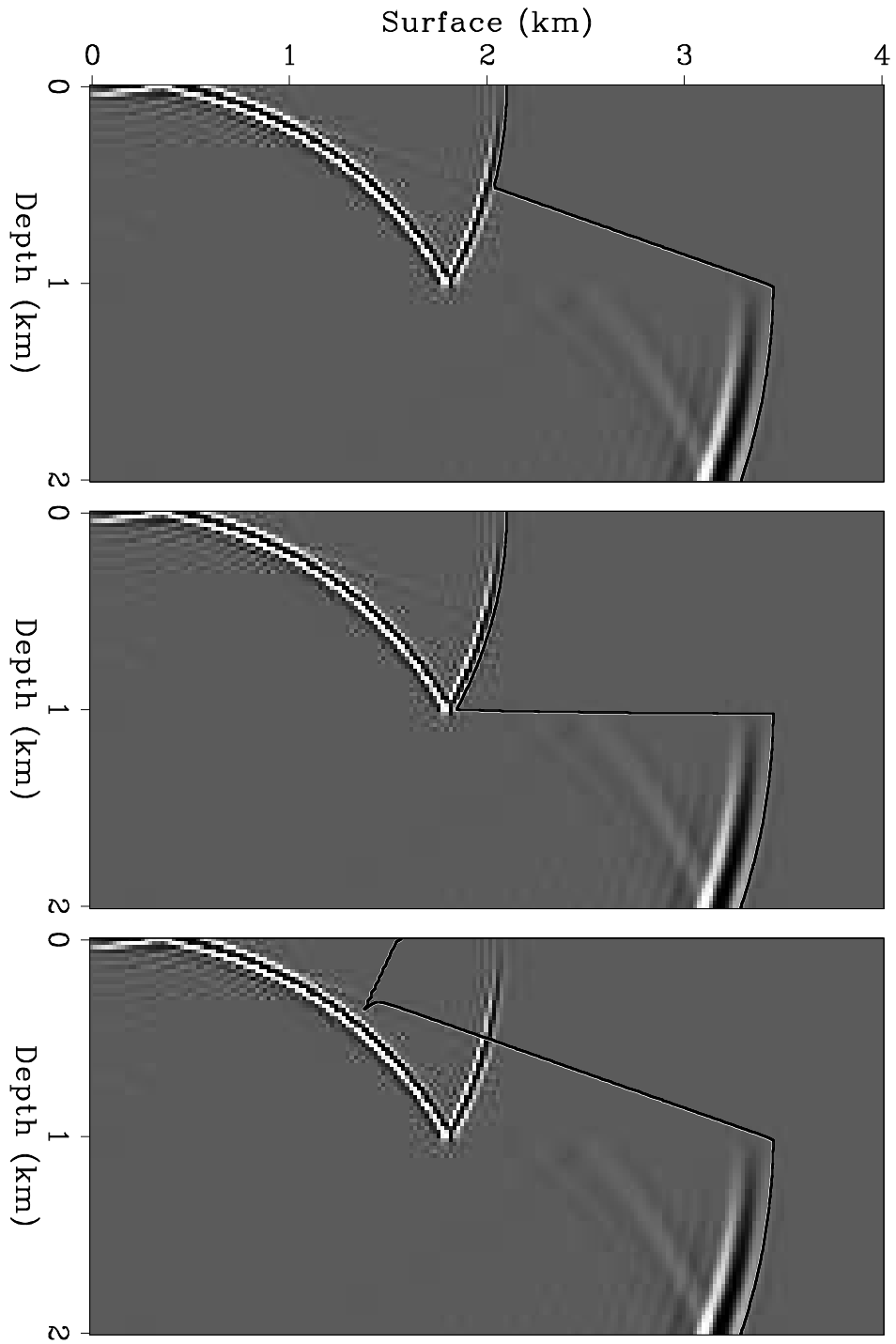

Figure 20: Comparison of the wave field simulated by wave-equation modeling with the traveltime fields calculated by the local ray-tracing method. The point source is positioned at the upper-left corner of the model. The intensity plots in three panels show a common snapshot of the wave field at 1.4 seconds; the overlain curves are the 1.4s-contour lines of three single-valued traveltime fields corresponding to first arrival (top), most energetic arrivals (middle), and upgoing arrivals (bottom), respectively. wftprg3-wavelay [ER]

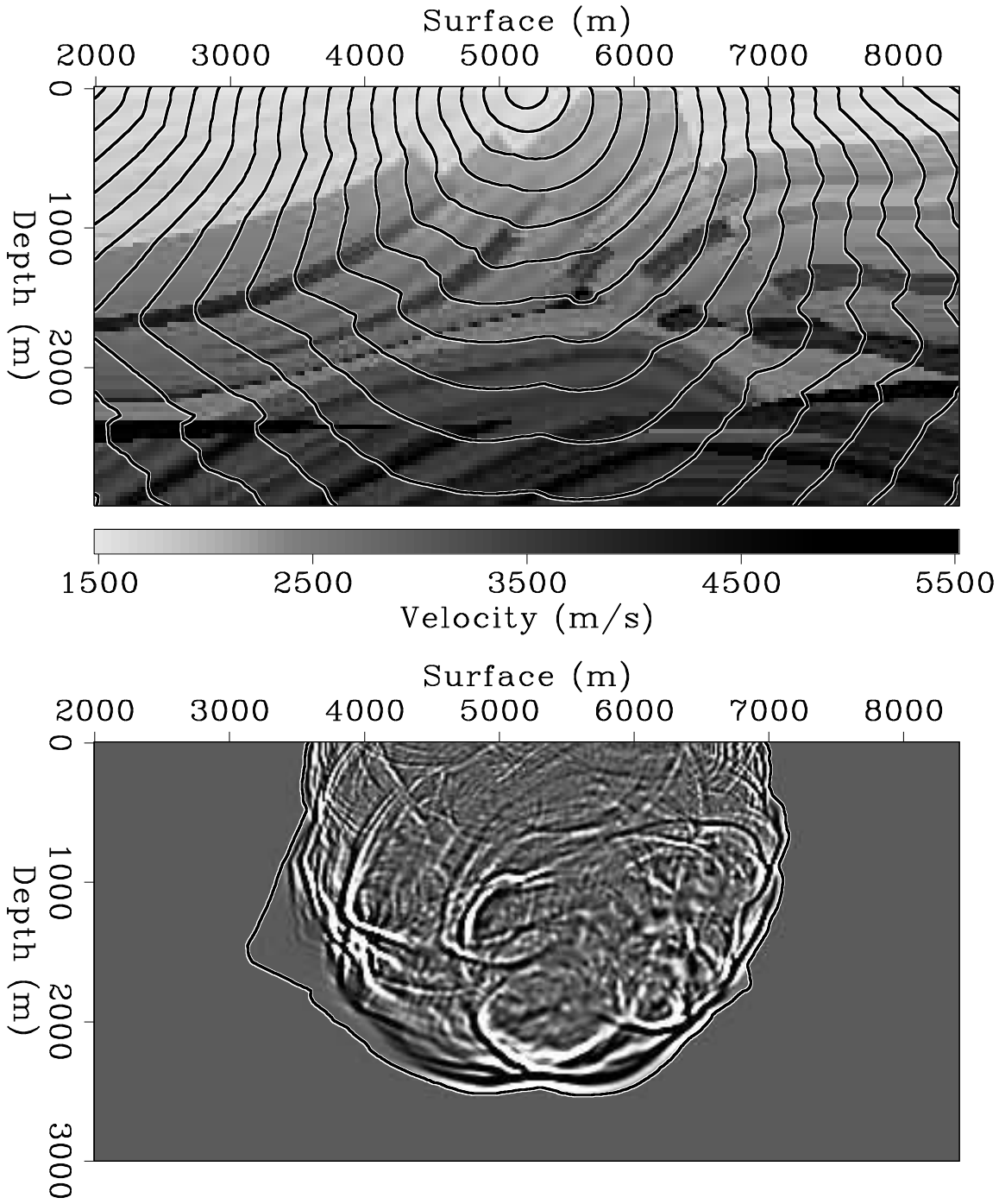

Figure 21: The traveltime field of first arrivals in the Marmousi model. The point source is positioned at the top center of the model. The top panel displays the velocity field. Overlain are the contour lines of the traveltime field with 0.1 second intervals. The bottom panel compares the wave field computed by wave-equation modeling with the traveltime field calculated by the local ray-tracing method. The intensity plot shows a snapshot of the wave field at 1.0 second; the overlain curve is the 1.0 second contour line of the traveltime field. wftprg3-twmar1 [ER]

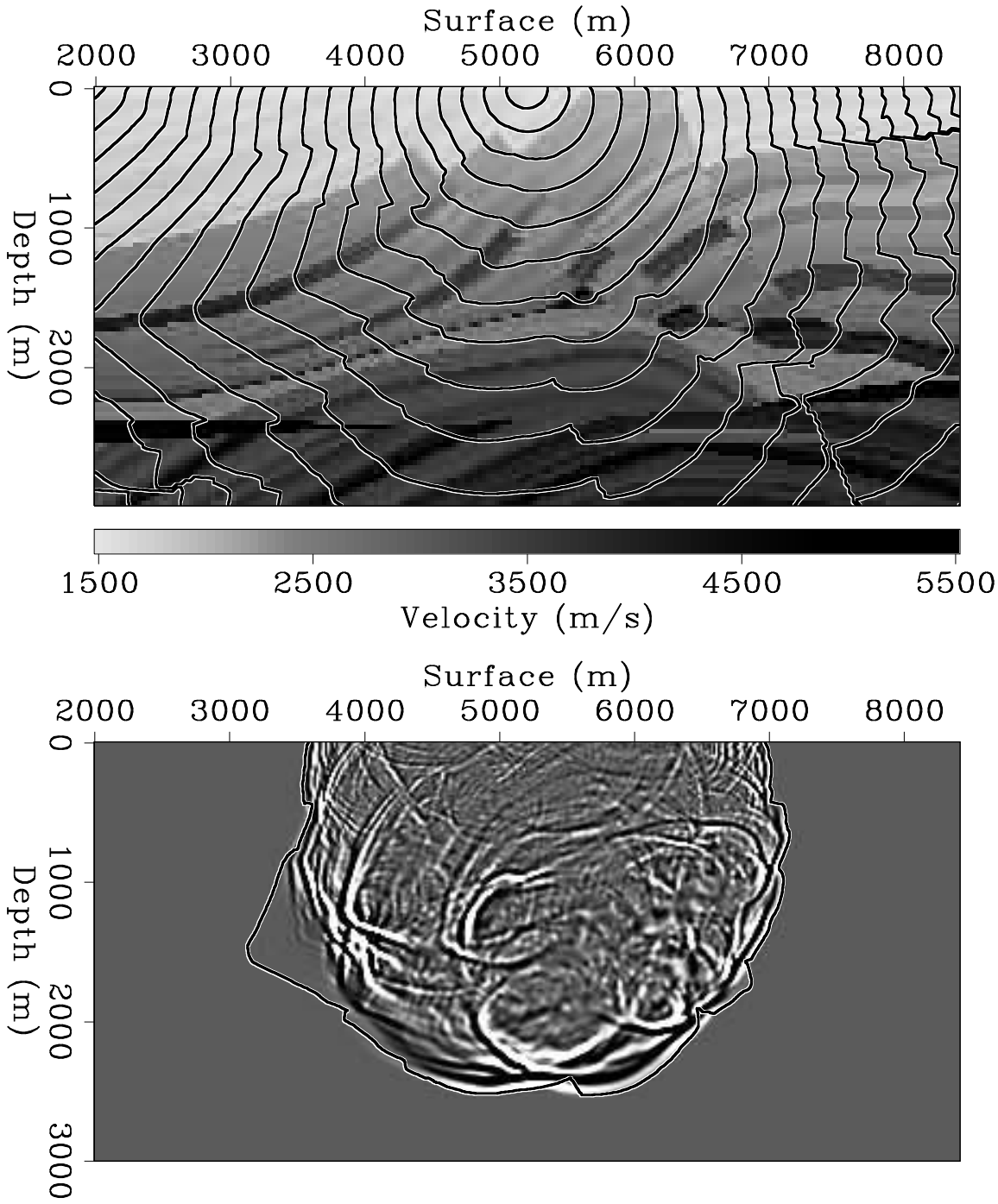

Figure 22: The traveltime field of most energetic arrivals in the Marmousi model. The point source is positioned at the top center of the model. The top panel displays the velocity field. Overlain are the contour lines of the traveltime field with 0.1 second intervals. The bottom panel compares the wave field computed by wave-equation modeling with the traveltime field calculated by the local ray-tracing method. The intensity plot shows a snapshot of the wave field at 1.0 second; the overlain curve is the 1. second contour line of the traveltime field. wftprg3-twmar2 [ER]

Summary

I have presented a new method, which I call the local ray-tracing method, for calculating the traveltimes and geometrical amplitudes of seismic waves in a two-dimensional velocity model. Because the method assumes a continuous velocity representation and propagates local circular wavefronts by following local rays, it is computationally more expensive, but gives more accurate traveltimes and amplitudes than the finite-difference method. The local ray-tracing method can also compute the traveltimes of multiple arrivals. But the selection of specific arrivals can only be done locally. I have evaluated the method with several synthetic velocity models and in each case checked the result with either analytical solutions or wave equation modeling. The traveltimes and amplitudes calculated by this method can be used in Kirchhoff depth migration.